Small Structures

www.small-structures.com

RESEARCH ARTICLE OPEN ACCESS

Stabilizing Lithium Metal Surface in Solid-State Batteries via Single-Step Gas-Phase Synthesis of Li_3N Interfacial Layer

Zhenghuan Tang[1] | Ayush Morchhale[1] | So-Yeon Ham[2] | Junbin Choi[1] | Lakshmi Surag Singavarapu[3] | Lalith Rao[1] | Minghao Zhang[4] | Christopher J. Brooks[5] | Ying Shirley Meng[4,6] | Jay R. Sayre[3] | Jung-Hyun Kim[1]

[1]Center for Automotive Research, Mechanical and Aerospace Engineering, The Ohio State University, Columbus, Ohio, USA | [2]Materials Science and Engineering Program, University of California San Diego, La Jolla, California, USA | [3]Materials Science and Engineering, The Ohio State University, Columbus, Ohio, USA | [4]Pritzker School of Molecular Engineering, University of Chicago, Chicago, Illinois, USA | [5]Honda Research Institute USA, Columbus, Ohio, USA | [6]Department of Nano Engineering, University of California San Diego, La Jolla, California, USA

Correspondence: Jay R. Sayre (sayre.17@osu.edu) | Jung-Hyun Kim (kim.6776@osu.edu)

Received: 31 January 2026 | **Revised:** 19 April 2026 | **Accepted:** 24 April 2026

Keywords: argyrodite electrolyte | DRT | Li anode | Li dendrite | Li_3N | PFIB | solid state batteries

ABSTRACT

The performance of solid-state Li-metal batteries (SSLBs) with argyrodite solid electrolytes (SEs) is limited by interfacial side reactions at the Li-metal/SE interface. In this study, we introduce Li_3N interfacial layer as a stabilizer at the Li/SE interface based on its good electrochemical and mechanical properties. The Li_3N is synthesized onto the Li-metal substrate in micrometer thickness through a straightforward treatment of Li-metal in a N_2-filled glovebox, as confirmed by plasma focused ion beam analysis. The Li_3N interfacial layer exhibits outstanding cycling stability in its symmetrical cell for over 5000 cycles, equivalent to 6000 h of operation, while the bare Li symmetrical cell endures only 257 cycles. Multimodal characterization techniques coherently demonstrate that the Li_3N interfacial layer contributes to reducing mechanical resistance (e.g., voids, microcracks) at the Li/SE interface, as well as charge–transfer resistance during cycling in full-cells, particularly when paired with $LiNbO_3$-coated $LiNi_{0.6}Mn_{0.2}Co_{0.2}O_2$ (NMC622) cathode. Furthermore, the Li_3N interfacial layer not only enhance specific capacity (178 mAh g^{-1}) and Coulombic efficiency (>99% at the 2^{nd} cycle) but also improve the rate capability of the SSLB full cells. Our study highlights the promising strategy of employing Li_3N as an interfacial layer for stabilizing the Li/SE interface in SSLBs.

1 | Introduction

In recent times, all solid-state Li-metal batteries (SSLBs) have gained substantial attention as the next-generation energy storage device because of their high energy density, improved thermal safety, and stability [1–4]. Over the past few decades, several types of solid electrolytes (SEs) have been developed, and Li-argyrodites (Li_6PS_5X, where $X = Cl$, Br, I) have emerged as a promising candidate owing to their high ionic conductivities that are comparable to that of Liquid electrolytes [3, 5, 6]. However, their practical application has been hindered by a few technical challenges (see Scheme 1). First, Li-argyrodite SEs are susceptible to reduction by Li metal or oxidation by cathode active materials due to their narrow electrochemical window (1.71 V–2.01 V), leading to the formation of a solid electrolyte interface (SEI) layer that significantly slows down Li-ion transportation at the interface and increases cell impedance [7]. Consequently, several Li-argyrodite-based SSLB systems exhibit huge capacity loss and low cycle efficiency [7–10]. Additionally, Li-argyrodite SEs suffers from Li-dendrite penetration over cycles [9, 11, 12]. Due to the high electrical and low ionic conductivities at grain boundaries, Li-ions and electrons are attracted to form metallic Li dendrite along grain boundaries [3, 7, 10, 13–15]. Moreover, voids are formed at the Li/SE interface under

Small Structures, 2026; 7:e70458
https://doi.org/10.1002/sstr.70458

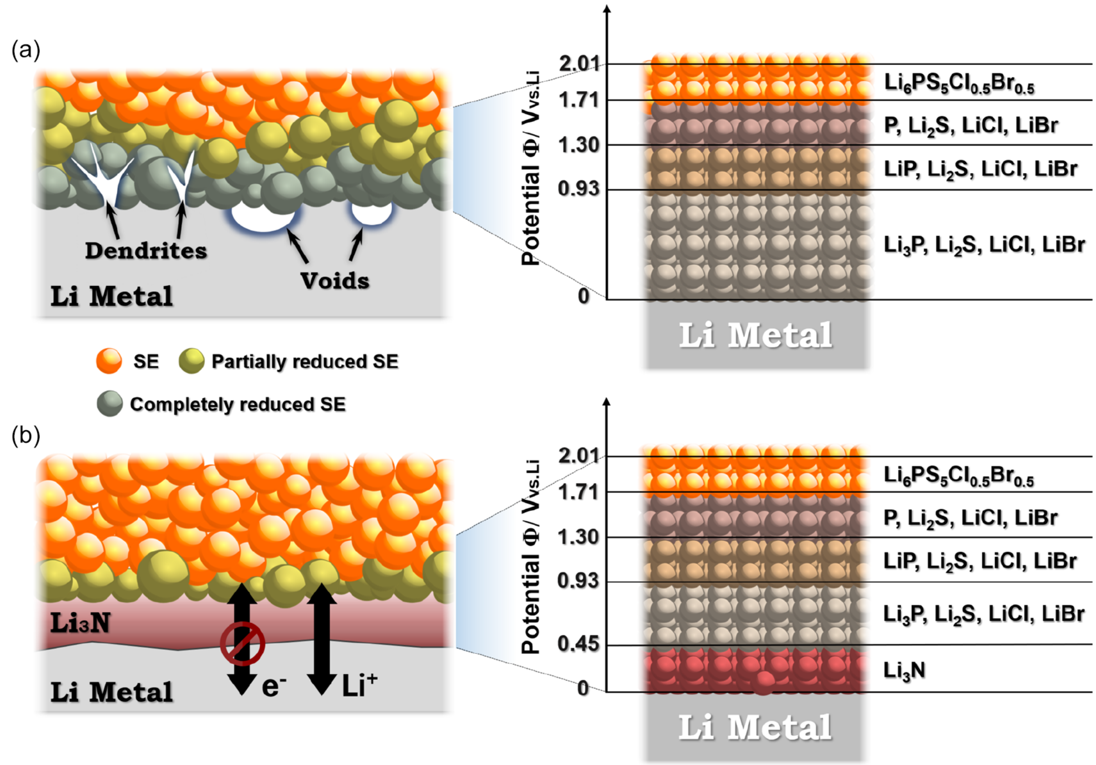

SCHEME 1 | Comparison of lithium deposition behaviors between (a) Li/SE interface with dendrite, voids, and thick SE decomposition interfacial layer, and (b) Li_3N-Li/SE interface enabling uniform Li^+ transport, blocking electron crossover, and suppressing dendrite growth with thinner SE decomposition interfacial layer. Equilibrium phases produced at Li/$Li_6PS_5Cl_{0.5}Br_{0.5}$ and Li/Li_3N/$Li_6PS_5Cl_{0.5}Br_{0.5}$ interfaces at different potentials. The values and phases were calculated and reported in literature [7].

high current density during Li-stripping [16]. Even after further plating, the voids cannot be fully replenished due to uneven deposition of lithium. The accumulation of the contact loss concentrates the current flow at the Li/SE interface and eventually accelerates the dendrite formation at those current hot spots [2].

To overcome the issues associated with Li-Argyrodite SEs in SSLBs, several strategies have been proposed, such as elemental doping [17–19], and in situ SEI formation [20, 21], and interlayer engineering [22–24]. Among these strategies, interlayer engineering has shown promising advantages due to its simple processing and scale-up friendliness. To stabilize the Li/SE interface, interlayer materials with a wide stability window are required to fill the stability gap between Li and SE and suppress side reactions at the interface [25]. Furthermore, the interlayer materials should have low electrical conductivity to prevent nucleation between Li-ions and electrons, as well as high ionic conductivity to allow for efficient transportation of Li-ions. Although various materials have been proposed as interlayers, Li-binary compounds have emerged as the most promising candidates. Li-binary compounds possess not only low electrical conductivities but also exhibit excellent stability with metal Li and wide stability windows at lower voltage against Li. Table 1 provides an overview of the key properties of various interlayer materials that have been reported in the literature.

TABLE 1 | Summary of Li^+ conducting interlayer candidates and their properties reported in Literature. Green color code for desired properties: $\sigma_{Li} > 10^{-4}$ S cm^{-1}, $\sigma_e < 10^{-10}$ S cm^{-1}, $E_{Li}^{SSE} > 0$. Yellow color code for acceptable properties: $10^{-4} > \sigma_{Li} > 10^{-7}$ S cm^{-1}, 10^{-10} S cm^{-1} $< \sigma_e < 10^{-8}$ S cm^{-1}. Red color code for undesired properties: $\sigma_{Li} < 10^{-7}$ S cm^{-1}, $\sigma_e > 10^{-8}$ S cm^{-1}.

Materials	$\sigma_{Li}{}^+$, S cm^{-1}	$\sigma_e{}^-$, S cm^{-1}	Stability with Li	Interface energy, meV Å^{-2}	Method
Li_2O	$\sim 10^{-9}$	Not reported	Good	Not reported	EIS [26]
LiCl/Li_3P	3.54×10^{-6}	Not reported	Good	Not reported	EIS [27]
LiI	2.8×10^{-8}	2.8×10^{-8}	Good	Not reported	EIS [23, 28]
LiF	3×10^{-9}	Not reported	Good	73.27	EIS [23, 29]
Li_3N	2×10^{-4}	10^{-12}	Good	32.13	EIS [22, 30]
Li_2S	10^{-5}	9.21×10^{-9}	Good	19.01	EIS [22, 31, 32]
Li_3P	10^{-4}	Not reported	Good	45.64	DFT [22, 33]

Li_3N has demonstrated its potential as an effective interlayer material in SSLBs [34, 35]. Li_3N SEI interlayer can stabilize the Li/SE interface in two distinct mechanisms (Scheme 1b). First, Li_3N SEI layer effectively reduces the electrochemical stability gap between Li and LPSCB, thereby mitigating decomposition reactions [7, 35]. Second, Li_3N showed good capability in suppressing dendrite growth and void formation. The combination of positive interface energy of Li_3N against Li (32.13 eV $Å^{-1}$) [22, 30], low Li-ion diffusion barrier of Li_3N (0.1 eV) [36], high ionic conductivity ($\sim 10^{-4}$ S cm^{-1}) [22, 30], and high interfacial adhesion energy (1.358 J m^{-2}) [37] promotes fast Li-ion diffusion through the Li/SE interface, allowing good wetting and tight physical contact at Li_3N-Li/SE interface [22, 30, 38]. Additionally, the low electronic conductivity of Li_3N ($\sim 10^{-12}$ S cm^{-1}) [22, 30] effectively impedes electron passage through the Li_3N SEI interlayer. The wide electrochemical window of Li_3N can fill the electrochemical window gap between Li and SE, thereby suppressing side reactions during cycling (Scheme 1) [7]. In addition, Li_3N has a greater Young's modulus (~48 GPa) [39] compared to Li-metal (~7.8 GPa) and argyrodite SE (~22 GPa), enabling it to resist creep-driven deformation at the Li/SE interface and thus improve mechanical stability during cycling [40]. Previous studies have shown that Li_3N interlayers and Li_3N powder-layer can improve the performance of Li-ion liquid cells [22, 30, 34, 39]. Recently, Li_3N powder-layer was reported to improve the performance of solid-state cells at elevated temperature (e.g., 50°C) [41]. However, applying the particle coating between Li and SE not only degrades interfacial contact between Li and SE, but also adds an extra fabrication step involving high pressure pressing, which is not manufacturing friendly. In addition, the evolution of Li dendrite growth was reported in scale > 10 μm [40, 42]. Therefore, the passivation of Li metal interfacing to SE requires micrometer-sized thickness rather than nanometer to provide strong interfacial robustness. In situ Li_3N—rich interlayer was reported to effectively passivate the Li/SE interface through the conversion of N-doped LPSCB SE [20, 35]. However, the N-doped LPSCB SE experienced higher impedance in bulk and grain boundary. To address these issues, this paper demonstrates a new approach toward facile one-step synthesis of Li_3N interfacial layer on Li metal anode using rapid solid-vapor reactions and investigates its impact on the Li-argyrodite-based SSLB cell performance at room temperature.

2 | Results and Discussion

2.1 | Synthesis of Li_3N Interfacial Layer on Li Anode

First, a Li foil was brushed in an Ar-filled glovebox to decrease the thickness of a natural SEI on fresh Li surface that consists of Li_2CO_3, Li_2O, and LiOH [43, 44] After brushing, the foil displaying a shiny surface was roll-pressed onto Cu-foil with a target thickness of 100 μm. Subsequently, the Li foil was transferred to a glovebox filled with N_2, where it underwent the following chemical reaction (1) and produces Li_3N on top surface for controlled durations ranging from 1 to 6 min (Scheme S1) [30].

$$6Li + N_2 \rightarrow 2Li_3N \tag{1}$$

The development of the Li_3N interlayer was readily apparent due to the resulting discoloration, as shown in Scheme S1. Cross-section SEM and EDS map were obtained by plasma focused ion beam (PFIB), and the images (Figure 1a) clearly showed a dense Li_3N interfacial layer formed on top of the Li metal. The thickness of Li_3N interfacial layer was influenced by the exposure time in N_2; longer exposure times resulted in thicker Li_3N interfacial layer. The mass changes associated with Li_3N formation on the Li metal surface are summarized in Table S1. The results show a clear trend of increasing electrode mass as the N_2 exposure time increases from 1 to 6 min. The Li_3N interlayer is produced more quickly during the initial stage, driven by a rapid surface reaction following Equation (1). Following the formation of the Li_3N interfacial layer, the reaction rate became predominantly influenced by the slower Li^+ and N^{3-} solid-state diffusion, leading to a moderate thickening of the Li_3N interfacial layer during the period from 1 to 6 min. Samples exposed for 1 and 3 min retained good interfacial contact between Li and the Li_3N interfacial layer, whereas visible interfacial gaps appeared after 6 min of N_2 exposure. Therefore, subsequent experiments were conducted using the 3 min Li_3N-Li sample due to its good interfacial quality and reproducibility. The presence of Li_3N interfacial layer on Li surface was characterized using X-ray diffraction (XRD). In Figure 1b, the Li_3N-Li foil revealed peaks at 23.2°, 28.2°, 47.1°, and 52.3°, which correspond to the (001), (100), (002), and (110) planes in α-Li_3N phase (space group (S.G.): *P*6/*mmm*) [45, 46]. Due to the thin nature of the Li_3N layer, diffraction signals from the underlying Li metal substrate were also observed at 36.4°, 43.3°, and 65.4° [47]. Additionally, weak peak from Cu current collector was detected at 43.2°, 50.5°, and 74.2°, likely due to minor physical defects at the edges of the punched electrode. These XRD peaks were consistently observed across all Li_3N-Li samples exposed to N_2 for 1, 3, and 6 min (Figure S1).

The Li_3N-Li film was further characterized using X-ray photoelectron spectroscopy (XPS) is shown in Figure 1c. All the XPS spectra were fitted using Shirley peak background and the full width at half maximum (FWHM) values are reported in Table S2. Strong Li_3N peaks were clearly observed at 398.7 eV from N 1s spectra, and the relative area under this peak showed a minor increase of 12% after 6 min of Ar-etching [48]. Additional peaks associated with LiOH, Li_2CO_3, and Li_2O were observed in the O 1s spectra (Figure S2) at 531.8, 531.1, and 528.6 eV, respectively [44, 49, 50]. Upon etching, the relative area of the Li_2CO_3 peak decreased by 15.2%, while that of Li_2O increased by 41%, and LiOH showed a relatively small increase of 2%. In the Li 1s spectrum, Li_2CO_3 and Li_3N were identified at 55.7 eV and 54.8 eV, respectively, while the peak associated with a combination of Li_2O and LiOH appeared at a lower binding energy of 54.1 eV [43, 44, 49–53]. In the Li 1s spectra, Li_2CO_3 showed a decrease of 22% upon etching, while Li_3N and Li_2O/LiOH peaks grew by 15.1% and 45%, respectively. These secondary phases, commonly found on the Li metal surface as inherent natural SEI species difficult to remove completely, may also result from minor sample contamination during transfer and characterization in an open atmosphere [43, 44, 49, 54]. For instance, Figure S3 shows only trace amount of oxygen across the surface of thick Li_3N film due to sample loading. After 6 min of Ar^+ etching, Li_3N signal in the N 1s spectrum increased due to the removal of the natural SEI layer. In parallel, the Li 1s

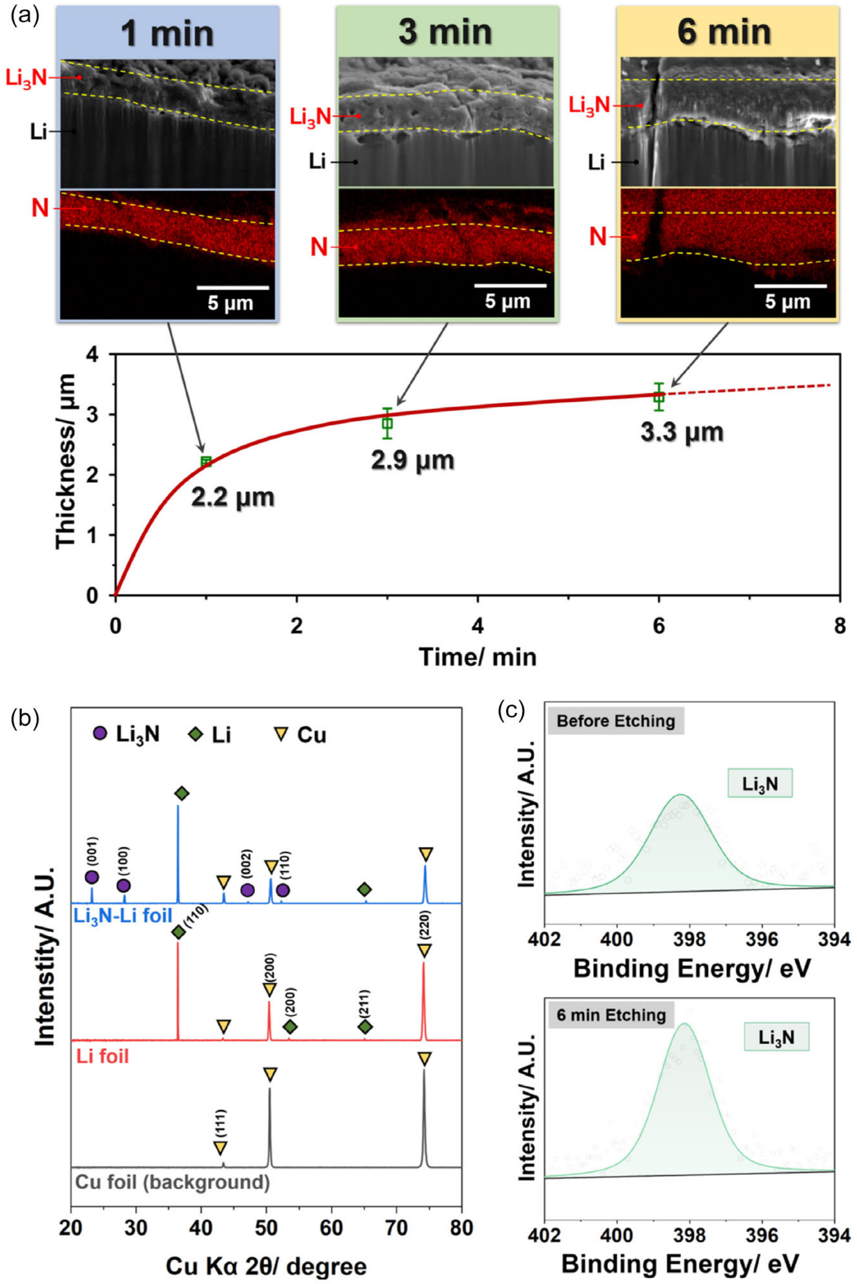

FIGURE 1 | (a) Cross-sectional PFIB-SEM-EDX images and respective thickness of the Li_3N-Li interface for exposure times of 1, 3, and 6 min in N_2, (b) XRD data of Cu foil, Li foil, and Li_3N-Li surface after 3 min N_2 exposure, and (c) XPS data showing N 1s spectra obtained from the pristine and 6 min Ar-etched (4000 eV) Li_3N-Li anodes. Prior to analysis, all XPS data were calibrated using the C─C bond peak at 284.8 eV as a reference.

spectrum indicated a reduction of Li_2CO_3 peak intensity, while stronger Li_3N, LiOH, and Li_2O signals emerged. It is challenging to completely eliminate these native SEI species from commercial Li metal surfaces, as mechanical brushing can disturb the surface but does not fully remove the pre-existing SEI layer. Overall, the combined SEM-EDX, XRD, and XPS data collectively confirm the successful formation of a thin, dense, and uniform Li_3N interfacial layer on the Li metal substrate.

2.2 | Symmetrical Cell Performances

The propagation of Li-dendrites is notably observed when the current density surpasses the threshold known as critical current density (CCD), a key indicator of the maximum current density a cell can endure without an internal short circuit [10]. The CCD testing has been widely adopted to examine the tolerance of SE within a cell against the Li-dendrite penetration [55, 56]. The “failure” or ‘short-circuit’ criterion in symmetric cell CCD test was defined as a sudden and irreversible voltage drop during a given current step, indicating internal short-circuit by Li dendrite penetration. The uncoated Li symmetrical cell experienced partial short-circuits at a current density of 0.9 mA cm^{-2} (Figure 2a). Consequently, its CCD value was determined to be 0.8 mA cm^{-2}, aligning with CCD values reported in literature [6, 22, 57]. On the other hand, the symmetrical cell fabricated with Li_3N-coated Li metal (i.e., Li_3N-Li Symmetrical cell) demonstrated an increased CCD value of 1.1 mA cm^{-2}

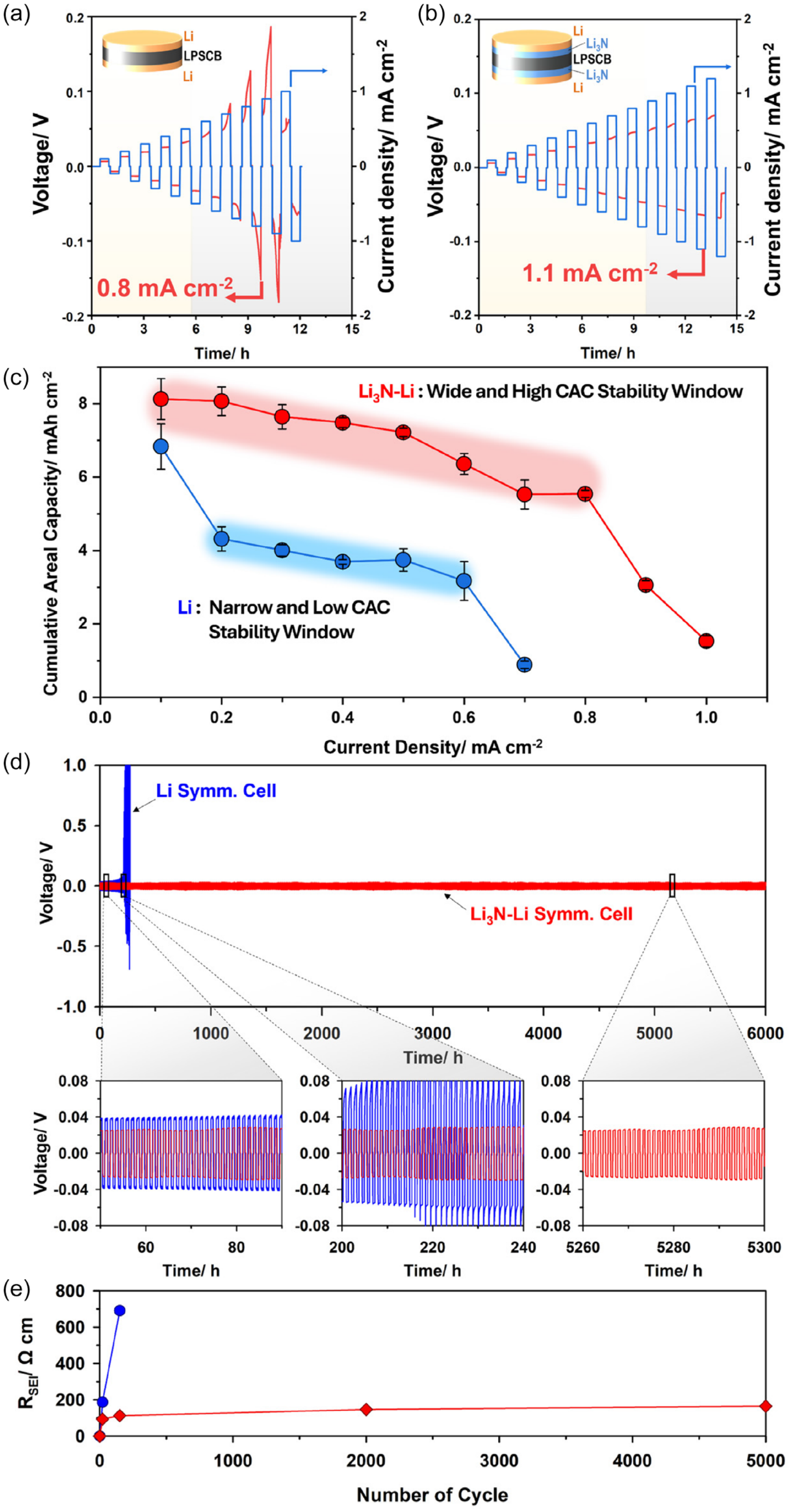

FIGURE 2 | CCD test of (a) Li/SE/Li and (b) Li/Li_3N-3min/SE/Li_3N-3min/Li symmetrical cells at RT. (c) Cumulative areal capacity (CAC) test of multiple symmetrical cells (at least 3 cells per data point) obtained by applying constant-current until cell failure by short circuits (corresponding voltage profiles are shown in Figure S6). (d) Cycling voltage profiles of Li and Li_3N -Li symmetrical cells under current pulses of ± 0.3 mA cm^{-2} for 30 min per step, and (e) corresponding evolution of R_{SEI} during cycling. All the measurements were performed at RT with an applied stack pressure of 5 MPa.

(Figure 2b). The symmetrical cells with Li_3N-1 min (Figure S4a) and Li_3N-6 min (Figure S4b) samples showed a CCD of 1.1 and 1 mA/cm^2, respectively. These results present a clear thickness-performance relationship where CCD improves with increasing Li_3N layer thickness up to ~2.9 µm (3 min), beyond which performance slightly declines. The reduction in CCD at 6 min is attributed to the mechanical stress-induced interfacial gaps observed in Figure 1a.

In addition to its higher CCD value, the Li_3N-Li symmetrical cell exhibited significantly more stable voltage profiles compared to the uncoated Li symmetrical cell. In Figure S5, we compared the relative overpotential increase during each CCD step. At 0.1 mA cm^{-2}, both cells showed similar but higher relative overpotential increase due to the activation of the fresh symmetrical cells. Until 0.4 mA cm^{-2}, both cells showed similar overpotential increase. Notably, the Li symmetrical cell demonstrated a significant increase in overpotential at current densities above 0.5 mA cm^{-2}, and it showed an abrupt 121% increase at 0.8 mA cm^{-2}. In contrast, the Li_3N-Li symmetrical cell maintained a much more stable interface, with the overpotential increase remaining below 7% throughout the higher current density range (0.5–1.1 mA cm^{-2}). This abrupt variation in voltage profile is attributed to the dynamic evolution of the Li/SE interfaces during repeated Li stripping/plating cycles. Stripping Li at high current densities can produce voids at the Li/SE interface, leading to a partial contact loss and a consequent increase in interfacial resistance (see Scheme 1) [16]. Often, this contact loss is not fully recovered during the subsequent plating process, causing current densities to concentrate on reduced interfacial areas, which further exacerbates interfacial contact issues and accelerates dendrite formation. This can lead to premature cell short-circuiting in the bare Li symmetrical cell. In contrast, the Li_3N-Li symmetrical cell maintained substantially more stable voltage profiles without sudden overpotential increases during repeated cycling up to 1.1 mA cm^{-2}, showcasing an increase of 38% compared to pure Li. This result suggests that the Li_3N interfacial layer between Li and SE preserves a stable interface throughout the cycles.

Although CCD test is generally accepted to quantify the suppression ability against Li dendrites, the CCD value is highly sensitive to various factors such as SE, Li metal, cell die parameters and testing protocols. The CCD testing, which applies bidirectional current in symmetric cells, often induces void at the Li/SE interface during Li stripping. This leads to concentrated local Li^+ flux and promotes dendrite growth during subsequent plating, resulting in an underestimation of the effective CCD.

To address this limitation, we recently proposed and demonstrated an alternative testing protocol: cumulative areal capacity (CAC) test. In the CAC test, each symmetrical cell is subject to unidirectional galvanostatic current until cell failure (Figure S6). A series of cells are tested, each under a different applied current density, and their respective CAC values at failure are recorded. By compiling results from multiple cells, CAC versus current density relationship is established. Figure 2c compares the CAC values of Li_3N-Li and Li symmetrical cells across various current densities. At a given current density, the Li_3N-Li symmetrical cells exhibited approximately twice the CAC values of the uncoated Li cells, indicating improved tolerance against short-circuit failure. In addition, the Li_3N-Li symmetrical cells maintained stable CAC values (8–6 mAh cm^{-2}) across a broad current density range of 0.1–0.8 mA cm^{-2}, indicating a wide CAC stability window. In contrast, the uncoated Li symmetrical cells exhibited lower stable CAC values (4–3 mAh cm^{-2}) in a narrow CAC stability window (0.2–0.6 mA cm^{-2}). These results suggest that employing the Li_3N interfacial layer can approximately double the cathode loading in SSLBs compared to uncoated Li-metal anode, as evidenced by the increased CAC values. Furthermore, the Li_3N interfacial layer can tolerate 33.3% higher current density (0.8 mA cm^{-2}) than the uncoated Li-metal (0.6 mA cm^{-2}).

As a next step, we investigated the impact of the Li_3N interfacial layer on the lifespan of symmetrical cells by cycling under a current density of 0.3 mA cm^{-2}and a capacity of 0.15 mAh cm^{-2}. Bare Li symmetrical cell showed a steady increase in voltage profile over the first 200 cycles. However, a significant voltage surge was recorded after 200th cycle, leading to eventual cell failure at 257th cycle. In stark contrast, the symmetrical cell with the Li_3N interfacial layer maintained a remarkably consistent voltage profiles over an extended period of 5000 cycles for 6000 h, as shown in Figure 2d.

In situ EIS and distribution of relaxation times (DRT) analysis were performed to elucidate the development of the Li/SE interface during the extended cycling of symmetrical cells. The analysis of the relationship between the DRT peaks and equivalent circuit model (ECM) is discussed in supporting information [58]. By deconvoluting major impedance sources from the data of pristine symmetrical cells, we could evaluate the aging behaviors of Li/SE interface throughout extended cycling. Figure 3 presents Nyquist plots and DRT curves at various cycling stages, referencing the same cells demonstrated in Figure S7. Their impedance values are also summarized in Table 2.

Before beginning the cycling tests, both the uncoated Li-symmetrical cell (with Li/SE/Li cell configuration) and Li_3N-Li symmetrical cell (with Li/Li_3N/SE/Li_3N/Li cell configuration) showed similar cell impedances. This result is consistent with the similar overpotentials (∼30 mV) recorded at the beginning of the cycling, as shown in Figure 2d. After the initial 20 cycles, both cells exhibited similar broader DRT peak emergence, indicative of SEI layer formation at the Li/SE interface [59, 60], resulting from the reductive decomposition of the argyrodite SE from chemical contact and electrochemical cycling [9, 61]. Analysis of the SEI layers and their chemical compositions will be discussed in following section. Additionally, the tail of the Nyquist plot extended, which resulted in the increase of the last peak in the DRT plot. This extension of tail indicated the slower kinetics of Li electrodeposition and dissolution from the SE/Li interface after cycles. In Figure 2d, the Li-symmetrical cell experienced a gradual increase in overpotential (∼40 mV), whereas the Li_3N-Li symmetrical cell consistently maintained its overpotential ∼30 mV.

At the 150th cycle, as discussed earlier, $R_{\mathrm{Li/SE}}$ emerged between 10^5 Hz and 10^4 Hz, indicating a degradation of Li/SE interface or microcracks within SE [16, 62]. When voids form at the Li/SE interfaces, current concentrates at localized contacts and promotes Li dendrite penetration along the grain-boundaries within SE [2]. The repeated Li plating/stripping at Li/SE interfaces exacerbates SEI degradation and unwantedly increases R_{SEI} from 266 Ω cm (20th cycle) to 352 Ω cm (150th cycle). As the cycling continued, a significant and abnormal rise in overpotential was observed in Figure 2d, attributed to the rapid rise in contact impedance and accelerated Li-dendrite growth, ultimately leading to the cell failure at the 257th cycle.

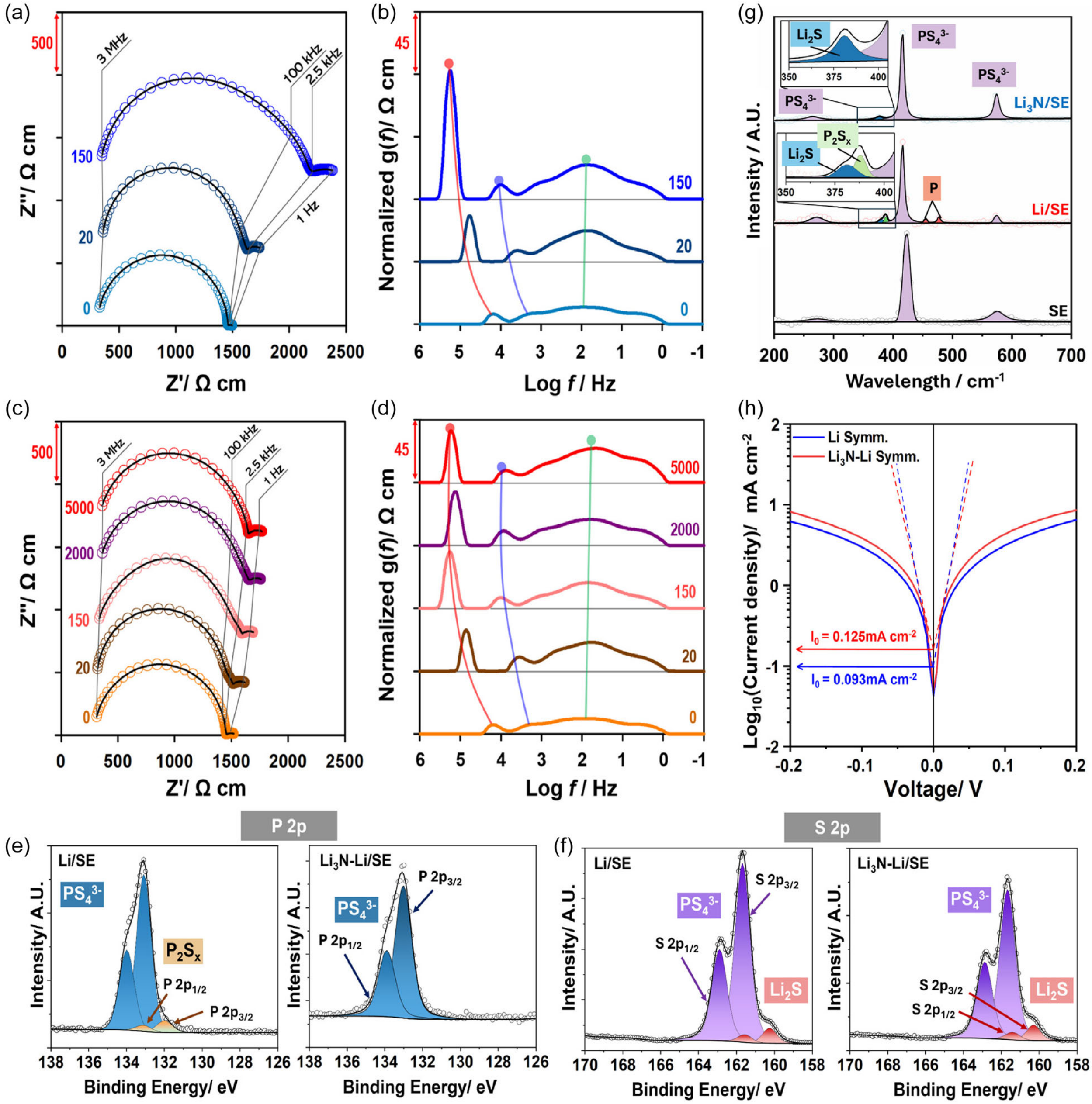

FIGURE 3 | Nyquist plots and corresponding DRT profiles of (a,b) Li symmetrical cell at 0th, 20th, and 150th cycles, and (c,d) Li_3N-Li symmetrical cell at 0th, 20th, 150th, 2000th, and 5000th cycles. XPS data showing (e) P 2p and (f) S 2p spectra obtained from Li/SE and Li_3N-Li/SE interfaces after 20 cycles. (g) Raman spectra of cycle-aged anode/SE interfaces from both symmetrical cells after 60 cycles with magnified SEI byproduct peaks. (h) Exchange current density values determined from Tafel plots for both symmetrical cells.

TABLE 2 | Summary of impedance values for Li and Li_3N-Li symmetrical cells at different cycle numbers.

	Li symmetrical cell				Li_3N-Li symmetrical cell			
Cycle number	R_b, Ω cm	R_{gb}, Ω cm	$R_{Interface}$, Ω cm	R_{void}, Ω cm	R_b, Ω cm	R_{gb}, Ω cm	$R_{Interface}$, Ω cm	R_{Void}, Ω cm
0	305	1152	89.1	—	290	1159	94.8	—
20	355	1176	265.6	—	297	1098	224.6	—
150	327	1169	352.3	691.4	330	1050	233.5	—
2000	—	—	—	—	305	1171	290.6	—
5000	—	—	—	—	332	1146	344.2	—

In stark contrast, the Li_3N-Li symmetrical cell preserved its stable Li/SE interface over 5000 cycles for about 6000 h. The DRT peak between 10^5 Hz and 10^4 Hz attributes to poor Li/SE contact never appeared for over 5000 cycles, indicating stable mechanical contact at the Li/SE interface throughout the testing. The SEI impedance experienced only a moderate increase from 224 Ω cm (20th cycle) to 344 Ω cm (5000th cycle). The cell also exhibited stable overpotential during the 5000 cycles. This significant improvement in cell performance can be explained by (1) reduced chemical potential gap across the Li–Li_3N–SE interface (Scheme 1), (2) enhanced wetting between Li and Li_3N, (3) suppressed electron transfer across the Li–Li_3N–SE interface, and (4) the strength of the Li_3N interfacial layer capable of withstanding repeated Li plating and stripping cycles, facilitated by its considerable thickness (nearly 3 μm), as illustrated in Figure 1a. These results highlight the effectiveness of the Li_3N interfacial layer in maintaining the stability of the Li–Li_3N–SE interfaces during the long-term cycling.

The chemical composition of the SEI layer at the Li/SE and Li_3N-Li/SE interfaces in symmetric cells were characterized by XPS after 20 cycles. The FWHM values of the fitted peaks are reported in Table S3. In the P 2p spectra (Figure 3e), only PS_4^{3-} ($2p_{3/2} = 132.9$ eV), attributed to the argyrodite SE, was observed at the cycled Li/Li_3N/SE interface. In contrast, the uncoated Li/SE interface exhibited additional peaks corresponding to P_2S_x ($2p_{3/2} = 132.1$ eV) species, comprising 7.06% of the total peak area. These have been reported as reductive decomposition products of the argyrodite electrolyte, forming a resistive interphase that hinders Li^+ transport [23, 63, 64]. In the S 2p spectra (Figure 3f), both cells exhibited strong PS_4^{3-} peaks ($2p_{3/2} = 161.7$ eV), attributed to the argyrodite SE, along with minor Li_2S peaks ($2p_{3/2} = 160.5$ eV) [51, 65, 66]. The relative area of the Li_2S-assigned peak was found to be ~1.5% higher at the Li/SE interface compared to the Li_3N/SE interface. Li_2S has been reported as a typical decomposition product of argyrodite SE in contact with Li metal, and its moderate ionic conductivity (~10^{-5} S cm^{-1}) does not significantly contribute to interfacial impedance [22, 31, 32]. Additionally, its relatively low electronic conductivity (~10^{-8} S cm^{-1}) can suppress continuous SE reduction at interfaces.

After 60 cycles of the symmetrical cells, the chemical composition of the SEI was analyzed using Raman spectroscopy. Voigt function was used to fit the Raman spectra for pure SE, Li/SE, and Li_3N/SE samples. The fitted spectra are shown in Figure 3g and the corresponding peak positions, component assignments, and FWHM values for all three samples are summarized in Table S4. Compared to the fresh LPSCB SE powder, which exhibited characteristic PS_4^{3-} peaks at 272.9 cm^{-1}, 422 cm^{-1}, and 575.4 cm^{-1} [57, 67], the uncoated Li symmetrical cell revealed the presence of Li_2S (377.9 cm^{-1}, 5.1%), P_2S_x (383.9 cm^{-1}, 7.7%), and P (454.9 cm^{-1} and 474.1 cm^{-1}, 11.8%) species at the Li/SE interface [67, 68]. The presence of these by-products indicates continuous degradation of the SE in contact with bare Li-metal during the extended cycling [69, 70], which is responsible for the significant increase in R_{SEI} values (Figure 2e). In stark contrast, the Li_3N-Li symmetrical cell exhibited only Li_2S peaks (380.1 cm^{-1}, 5.7%) which is consistent with the XPS results [67, 68]. This result suggests that Li_3N interfacial layer effectively suppresses parasitic reactions at the Li/Li_3N/SE interface and maintain stable R_{SEI} values over 5000 cycles, as shown in Figure 2e.

The Li_3N-Li interface exhibits enhanced electrochemical kinetics, as evidenced by a reduced Tafel slope in its symmetrical cell compared to uncoated Li cell. As shown in Figure 3h, the linear region of the Tafel plots reveals a smaller slope, indicating lower overpotential requirements and more efficient Li/Li^+ charge–transfer behavior. Furthermore, the Li_3N-Li cell demonstrates a higher exchange current density (0.125 mA cm^{-2}) than the Li symmetric cell (0.093 mA cm^{-2}), suggesting that the electrochemically stable Li/Li_3N/SE interface promotes more efficient charge transfer kinetics during Li plating and stripping.

To further evaluate the impact of the Li_3N interfacial layer at higher current densities, we conducted long-term cycling tests on both Li_3N-Li and uncoated Li symmetric cells under a 20 MPa stack pressure to suppress void formation [40, 58, 71, 72]. As shown in Figure S8, both cells were cycled sequentially at 0.4, 0.5, 0.6, and 0.7 mA cm^{-2}, with 400 cycles completed at each current density step. Under the elevated pressure, both cells exhibited relatively stable overpotentials due to reduced void formation at the Li/SE interface. The uncoated Li symmetric cell completed 400 cycles at 0.4 and 0.5 mA cm^{-2}. However, upon stepping to 0.6 mA cm^{-2}, the cell shorted after just 3 cycles, as evidenced by a sudden drop in overpotential. In contrast, the Li_3N-Li cell remained stable through the full 400 cycles at 0.6 mA cm^{-2} and continued cycling for over 2000 h, confirming the enhanced interfacial stability imparted by the Li_3N layer even under high current and mechanical stress [73, 74].

2.3 | SSLB Cell Performances

The success of the Li_3N interfacial layer in symmetrical cells led us to investigate its impact on SSLB cell performance. In SSLBs with argyrodite SE, both the SEI and cathode-electrolyte interface (CEI) layers have critical issues due to narrow electrochemical stability windows of the sulfide-based SE [5, 8]. Our approach included systematic combinatorial experiments to understand the influence of SEI and CEI passivation on cell performance. By comparing SSLB performance with bare Li metal to those with Li_3N-coated Li metal, we can examine the effect of SEI passivation. Similarly, a comparison between uncoated NMC and $LiNbO_3$ (LNO)—coated NMC can identify the impact of CEI passivation. The LNO coating is broadly acknowledged for its stabilizing effect on CEI in sulfide-based solid-state batteries [4, 43, 44]. Figure S9 demonstrates the uniform LNO coating on NMC cathode particles. Through various cathode-anode combinations, we systematically evaluated their impacts on the performance of SSLB cells.

a. We first evaluated Li/NMC cell with uncoated NMC and uncoated Li metal. This baseline configuration without any SEI and CEI passivation yielded an initial discharge capacity of 120 mAh g^{-1} and CE of 54% in the first cycle (Figure 4). Also, it experienced significant capacity fading over 20 cycles and notable voltage polarization, as evidenced in the dQ/dV profile (Figure S10).

b. Next, we examined the Li_3N-Li/NMC SSLB cell, pairing a Li_3N-coated Li metal anode with uncoated NMC cathode. This cell demonstrated an improved initial discharge capacity of 140 mAh g^{-1} and CE of 63% in the first cycle, showing enhanced capacity retention and stable dQ/dV profiles over repeated cycling, comparing to those of the Li/NMC cell.

c. Subsequently, we paired LNO-coated NMC cathode with an uncoated Li metal anode to fabricate the Li/ LNO-NMC cell. This configuration significantly increased the initial capacity to 167 mAh g^{-1} and CE to 72%, surpassing the performance of earlier two groups (above 1 and 2). This improvement highlights that CEI degradation at the NMC/SE interface is a primary factor in the performance degradation of the NMC/Li cell.

d. Finally, we passivated both the SEI and CEI by pairing Li_3N-coated Li metal anode and LNO-coated NMC cathode in a cell. The Li_3N-Li/LNO-NMC cell exhibited the most outstanding performance metrics, including an initial discharge capacity of 178 mAh g^{-1} and a CE of 78%. Notably, it reached CE value of over 99% by the 2nd cycle, while the Li/LNO-NMC cell took five cycles to achieve it. These increased capacity and CE values suggest the Li_3N interfacial layer's effectiveness in suppressing parasitic reactions at the Li/SE interface.

At 200th cycles, the Li_3N-Li/LNO-NMC cell maintained a discharge capacity of 127 mAh g^{-1}, retaining 74% of its initial capacity. In comparison, the Li/LNO-NMC cell held a discharge capacity of 119 mAh g^{-1}, preserving 71% of its initial capacity. Despite the Li_3N interfacial layer providing a capacity advantage over the uncoated cell, both cells exhibited similar overall capacity retention after 200 cycles, attributed to the slow cycling rate of C/10. Both Li_3N-Li/LNO-NMC and Li/LNO-NMC cells also deliver similar impedance values at 200th cycle; e.g., $R_{\mathrm{Total}} = 12{,}953$ and $13{,}115\ \Omega$, respectively (see Table S5).

Following the 200th cycle, both the Li_3N-Li/LNO-NMC and Li/LNO-NMC cells were subjected to continued cycling under an accelerated aging protocol. This protocol comprised five cycles at each of the following rates: C/3 (0.33 mA cm^{-2}), C/2 (0.5 mA cm^{-2}), and C/10 (0.1 mA cm^{-2}), applied to both charging and discharging. Their capacity retentions were plotted in Figure 4a. Both cells experienced a notable capacity reduction when the C-rate increased from C/10 to C/2, attributable to the substantial SE thickness (700 μm) in the SSLB cells. This issue can be addressed by optimizing the SE thickness in future studies.

Upon completing three rounds of accelerated aging (45 cycles in total), the Li_3N-Li/LNO-NMC cell delivered discharge capacity of 113 mAh g^{-1} at the C/10 rate, experiencing an average capacity loss of 0.27% per cycle. In comparison, the Li/LNO-NMC cell exhibited a more pronounced capacity loss rate of 0.5% per cycle and reached a discharge capacity of 96 mAh g^{-1} at the 245th cycle. Notably, during the final round of accelerated aging cycles (i.e., the 230th–240th cycles), especially at C/3 and C/2 rates, the Li_3N-Li/LNO-NMC cell consistently outperformed the Li/LNO-NMC cell. This comparison distinctly highlights the beneficial impact of the Li_3N interfacial layer on the energy and power density of SSLB cells.

In Figure 4d, the Nyquist plots for both cells are presented at their 200th and 245th cycles. Analysis of these plots, along with their associated DRT profiles shown in Figure S11, is based on our symmetrical cell data (see, Figure 4) and other previously reported data [62, 71, 75, 76]. The intersection at high frequencies ($f > 3$ MHz) on the Nyquist plots indicates the bulk resistance (R_b) of the SE. The first semicircles centered at ∼0.5 MHz in the Nyquist plots are attributed to the grain boundary resistance (R_{GB}) combined with chemical contact resistance at the NMC/SE interface (R_{CEI}) as identified as P_1 and P_2, respectively, in the DRT profiles. The second semicircle, widely spanning from 2.5 kHz to 10 Hz in the Nyquist plots, are attributed to the combination of mechanical ($R_{\mathrm{NMC/SE}}$) contact resistance at the cathode/SE interface [77, 78], mechanical contact ($R_{\mathrm{Li/SE}}$) and the Li/SE interface (R_{SEI}) resistances. According to the DRT profiles, P_3 and P_4 were the two major peaks within this broad frequency range. P_3 centered at 10^3 represents the mechanical contact between NMC active material and SE (R_{NMC}) [71], and P_4 centered between 10^2 and 10 Hz represents the combination of SEI resistance at the Li/SE interface (R_{SEI}) and the mechanical contact resistance at the Li/SE interface ($R_{\mathrm{Li/SE}}$) [71, 77]. The last semicircle, spanning from 10 Hz to 0.5 Hz, corresponds to the part of SEI resistance at the Li/SE interface (R_{SEI}) and charge transfer resistance from both cathode and anode interface (R_{CT}) [71]. The last peak P_5 centered between 1 Hz and 0.1 Hz in the DRT curve represents the charge transfer resistance from both cathode and anode interface.

After 3 rounds of accelerated aging, the Li_3N-Li/LNO-NMC cell showed clear advantage of capacity retention over the unmodified Li/LNO-NMC cell. The major factor was the protection of Li_3N interfacial layer in inhibiting cell resistance growth (Table S5), especially in $R_{\mathrm{Li/SE}}$, R_{SEI}, and $R_{\mathrm{C.T.}}$. Under high C-rate cycling, the uncoated Li/SE interface was more vulnerable to irreversible SE decomposition, and void evolution. Therefore, the Li/LNO-NMC cell showed more increase in the combined impedance of $R_{\mathrm{Li/SE}}$ and R_{SEI}. Moreover, since the Li_3N-Li/SE interface already showed good mechanical stability at higher current density in our previous (>0.5 mA cm^{-2}) in our CCD test (see Figure 2b), the growth of mechanical contact resistance ($R_{\mathrm{Li/SE}}$) was also lower in the Li_3N-Li/LNO-NMC cell. In fact, R_{CEI} in the Li_3N-Li/LNO-NMC cell maintained its value after 3 accelerated aging rounds whereas the Li/LNO-NMC cell experienced 15% increase. More importantly, the total charge transfer resistance ($R_{\mathrm{C.T.}}$) of Li_3N-Li/LNO-NMC increased 31%, significantly lower than the 64% increase observed in Li/LNO-NMC cell. In our ECM, total charge transfer resistance accounts for both anode and cathode. Since both cells used the same cathode, it is reasonable to consider the Li_3N interfacial layer helped the Li_3N-Li/LNO-NMC cell to have 33% less total charge transfer impedance growth compared to the unmodified Li/LNO-NMC cell. Because of less insulating SEI growth at the Li_3N-Li/SE interface, the kinetics of Li electro-deposition and electro-dissolution are faster at the anode interface in Li_3N-Li/LNO-NMC cell [62]. Therefore, the anode charge transfer resistance in the Li_3N-Li/LNO-NMC cell had significantly lower growth than the Li/LNO-NMC cell did. Both cells experience slight and similar increase in R_{CEI} at the cathode/SE because the LNO coating at the NMC particles has been proven to effectively mitigate the CEI degradation. Additionally, the bulk SE (R_B), grain boundary (R_{GB}) impedances remained stable, as both cells used the same SE material. The lesser increase in cell

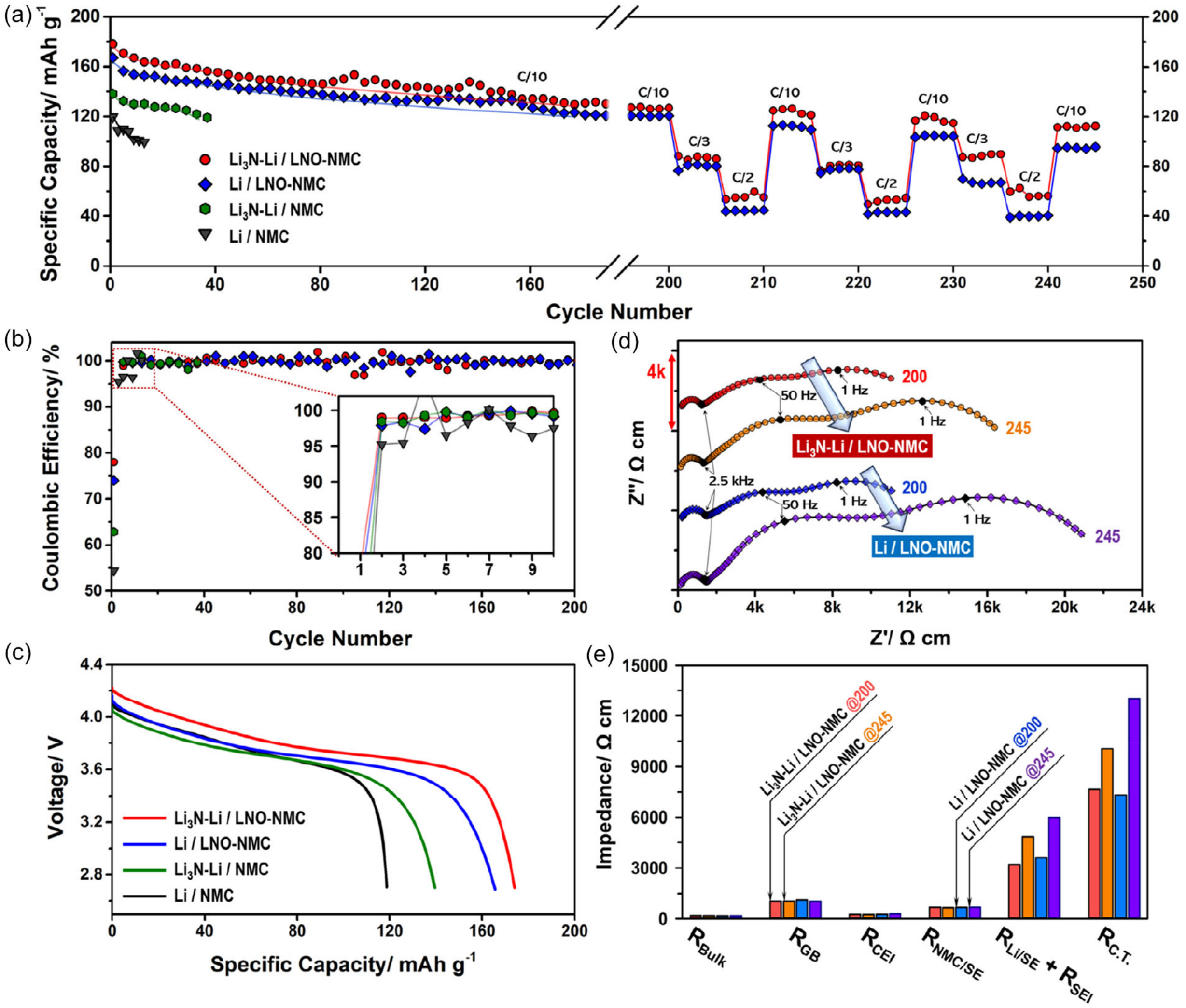

FIGURE 4 | (a) Effect of Li-metal coating with Li_3N layer and NMC622 cathode coating with $LiNbO_3$ (LNO) on cycle life (first 200 cycles at C/10, 0.1 mA cm^{-2}) and rate performance (post 200 cycles). Various combinations of coated and uncoated electrodes were tested in SSLB cells at RT. (b) Corresponding Columbic efficiencies and (c) initial discharge voltage profiles. (d) Nyquist plots and (e) extracted impedance values of Li_3N-Li/LNO-NMC and uncoated Li/LNO-NMC SSLB cells at the 200th and 245th cycle.

resistance in the Li_3N-Li/LNO-NMC cell provided evidence that Li_3N interfacial layer effectively mitigated the Li/SE interface deterioration, thus explaining the capacity advantage over the Li/LNO-NMC cell can be explained by the lower impedance increase, which leads to better cell performance. While the capacity difference between the Li_3N-Li/LNO-NMC and Li/LNO-NMC cells initially showed a trend to converge, the accelerated aging cycling eventually resulted in a divergence in capacity difference. These findings highlight the potential of the Li_3N interfacial layer as a promising strategy for enhancing the cycling stability and performance of SSLBs during higher C-rate operations.

3 | Conclusion

This study focuses on the facile one-step synthesis and application of Li_3N interfacial layer in Li-argyrodite SSLB systems. Li_3N interfacial layer is successfully synthesized within the N_2 glovebox environment by a facile one-step solid-vapor reaction. In both Li symmetrical cell and SSLB full cell testing, the Li_3N interfacial layer demonstrates remarkable impact on stabilizing the Li/SE interface by preventing Li dendrite penetration, suppressing side reactions, and maintaining physical contact. Notably, the Li_3N-Li symmetrical cell exhibits a 20% higher CCD value and demonstrates an extended plating/stripping life, cycling for over 5000 cycles compared to the uncoated Li symmetrical cell, which fails after 257 cycles. XPS and Raman analysis further confirms the ability of the Li_3N interfacial layer in suppressing SE decomposition at the Li/SE interface. Moreover, SSLB full cell testing reveals improvements in cell capacity and efficiency with the Li_3N interfacial layer compared to the unmodified Li/LNO-NMC cell. Under C/10-rate testing conditions, SSLB full cell with Li_3N interfacial layer consistently maintains ~10 mAh g^{-1} more capacity than the unmodified cell over 200 cycles. Additionally, both CCD and SSLB full cell accelerated aging tests demonstrate the ability of Li_3N interfacial layer in stabilizing Li/SE interface in relatively high C-rate cycling conditions. Future work will focus on optimizing parameters of Li_3N interfacial layer including interfacial layer thickness, mechanical properties of films, and their relationship to electrochemical performance.

4 | Experimental Section

4.1 | Fabrication of Li_3N Interlayer onto Metallic Li Anode

Li_3N interfacial layer was achieved by chemical vapor deposition method. Referring to Schematic S1, a Li foil with was first mechanically cleaned and rolled into 100 μm in an Ar-filled glovebox. The cleaned Li foil, was then transferred into a N_2-filled glovebox (Plas-Labs) and mechanically cleaned again until the surface turns black, indicating the formation of Li_3N on the Li surface. The Li_3N-coated Li foil was then quickly transferred back into the Ar-filled glovebox and punched out into a disk with a diameter of 9 mm.

4.2 | $LiNbO_3$ (LNO) Coating onto $LiNi_{0.6}Co_{0.2}Mn_{0.2}O_2$ (NMC622) Cathode

The $LiNbO_3$ coating was applied to the NMC622 (MSE Supplies) powders by sol–gel method. $Li(CH_3COO)$ (Acros Organics) and $Nb(OCH_2CH_3)_5$ (Acros Organics) were dissolved in ethanol and mixed with NMC622 powder overnight. Then, the solution was ultrasonicated for 15 min followed by drying in an oven. Finally, the resulting powder was heated at 450°C for 20 h in air. The resulting LNO-coated NMC622 powders, $Li_6PS_5Cl_{0.5}Br_{0.5}$ (LPSCB, Ampcera) powders, carbon black, and polystyrene-block-poly(ethylene-ran-butylene)-block-polystyrene (SEBS, Sigma Aldrich) binder were mixed with Butyl Butyrate (Sigma Aldrich) to form slurry. The slurry was then casted onto Al foil and dried at room temperature overnight. The active material loading was estimated to be 4.8 mg cm^{-2}.

4.3 | SSLB Cell Fabrication

For Li-symmetrical cell, 100 mg LPSCB powder was pressed under 500 MPa for 6 min into a 10-mm cell die. A 100 μm Li foil was first mechanically cleaned and then punched into two 9 mm disks and pressed to both sides of the SE at 150 MPa for 30 s. For NMC full cell, 100 mg LPSCB powder was first pressed under 150 MPa to form a loose pellet. Then a 10 mm LNO-NMC cathode was inserted into the pellet die and pressed under 500 MPa with the existing bulk pellet. One 9 mm Li disk was punched out and pressed to the other side of the SE at 150 MPa for 30 s. Both symmetric cells (used for CCD, CAC, and long-term cycling tests) and NMC full cells were assembled and tested at a stack pressure of 5 MPa using a constant-distance cell design (nuts and bolts) throughout all electrochemical measurements.

4.4 | Sample Characterization

Plasma focused ion beam scanning electron microscope (PFIB-SEM, ThermoFisher Scientific Helios 5 Hydra) was used to obtain large cross-sectional images. For rough milling, a Xe^+ ion beam with a setting of 30 kV and 500 nA was employed to broadly mill the samples. Subsequently, the beam current was adjusted to a lower value of 200 nA to clean the cross-sections. Scanning electron microscope (SEM) and energy dispersive X-ray spectroscopy (EDX) attached to the PFIB were used for the image acquisition and EDS elemental mapping with the electron beam parameter set to 5 kV and 0.10 nA. SEM (Hitachi S-3000H) images were obtained with an acceleration voltage of 15 kV. Electrochemical impedance spectroscopy (EIS, Gamry 1010E) of selected cells were obtained in a frequency range of 3 MHz–1 Hz, and the resulting data was analyzed by DRT software in MATLAB developed by Wan et al. [79] using default setting (Method of Discretization: Gaussian, Regularization parameter: 10^{-3}, Fitting with Inductance, and 1st order regulation derivative). Tafel plot (Gamry 1010E) were obtained using scan rate of 1mV/s within the range of −0.15 V to 0.15 V. Phases of synthesized materials were characterized using XRD measurement (Rigaku SmartLab with Cu-Kα radiation). Raman Spectroscopy spectrums (Renishaw Raman IR Microprobe) were obtained with a wavelength of 514 nm. XPS (Nexsa G2) with Ar^+-etching was conducted at the surface of Li_3N-Li foil. The CCD value of Li—symmetrical cell was obtained by galvanostatic cyclic measurements starting from 0.1 mA $cm^{-2}$with a step increase of 0.1 mA cm^{-2}. Each step had a 30 min charging, a 30 min discharging, and 5 min rest between each of the events. The cell was cycled in Ar-filled glovebox (i.e., continuous stripping and plating) at a current density of 0.3 mA cm^{-2} with the capacity limit of 0.15 mAh cm^{-2} at 25 °C.

Author Contributions

Zhenghuan Tang: Conceptualization, Data curation, Methodology, Project administration, Validation, Visualization, Writing – original draft, Writing – review & editing. **Ayush Morchhale**: Investigation, Data curation, Methodology – XRD, XPS, EIS and DRT. **So-Yeon Ham**: Investigation, Validation, Methodology – PFIB and EDS, Data curation, Writing – original draft, Writing – review & editing. **Junbin Choi**: Investigation, Methodology – Raman Spectroscopy, Validation, Visualization, Data curation. **Lakshmi Surag Singavarapu:** Investigation, Methodology – XPS, Validation, Visualization, Data curation. **Lalith Rao:** Investigation, Methodology – XRD, Validation, Visualization, Data curation. **Minghao Zhang**: Investigation, Validation, Methodology – PFIB and EDS, Data curation, Writing – original draft, Writing – review & editing. **Christopher J. Brooks**: Conceptualization, Project administration, Resources, Supervision. **Ying Shirley Meng**: Project administration, Resources, Supervision. **Jay R. Sayre**: Conceptualization, Project administration, Resources, Supervision. **Jung-Hyun Kim**: Conceptualization, Methodology, Project administration, Supervision, Writing – original draft, Writing – review & editing.

Acknowledgments

This work was supported by Honda Research Institute USA. This work at UChicago was supported by the Energy Transition Network (ETN) at the Institute for Climate and Sustainable Growth (ICSG).

Funding

This work was supported by Honda Research Institute USA and the Energy Transition Network (ETN) at the Institute for Climate and Sustainable Growth (ICSG).

Conflicts of Interest

The authors have no conflicts of interest.

Data Availability Statement

The data that support the findings of this study are available from the corresponding author upon reasonable request.

References

1. H.-J. Deiseroth, S.-T. Kong, H. Eckert, et al., "Li_6PS_5X: A Class of Crystalline Li-Rich Solids With an Unusually High Li^+ Mobility," *Angewandte Chemie International Edition* 47 (2008): 755.

2. Z. Tang, J. Choi, J. L. Lorie Lopez, et al., "Optimization of the Li_3BO_3 Glass Interlayer for Garnet-Based All-Solid-State Lithium–Metal Batteries," *ACS Applied Energy Materials* (2022): acsaem.2c01606.

3. C. Yu, F. Zhao, J. Luo, L. Zhang, and X. Sun, "Recent Development of Lithium Argyrodite Solid-State Electrolytes for Solid-State Batteries: Synthesis, Structure, Stability and Dynamics," *Nano Energy* 83 (2021): 105858.

4. H. Huang, J. Jin, C. Zheng, et al., "Bonded Interface Enabled Durable Solid-state Lithium Metal Batteries with Ultra-low Interfacial Resistance of 0.25 Ω Cm^2," *Advanced Functional Materials* 34 (2024): 2407619.

5. A. Morchhale, Z. Tang, C. Yu, R. Farahati, and J.-H. Kim, "Coating Materials and Processes for Cathodes in Sulfide-Based All Solid-State Batteries," *Current Opinion in Electrochemistry* 39 (2023): 101251.

6. G. Liu, W. Weng, Z. Zhang, L. Wu, and J. Yang, "Densified Li_6PS_5Cl Nanorods with High Ionic Conductivity and Improved Critical Current Density for All-Solid-State Lithium Battery," *Nano Letters* 20 (2020): 6660–6665.

7. Y. Zhu, X. He, and Y. Mo, "Origin of Outstanding Stability in the Lithium Solid Electrolyte Materials: Insights from Thermodynamic Analyses Based on First-Principles Calculations," *ACS Applied Materials and Interfaces* 7 (2015): 23685.

8. J. Auvergniot, A. Cassel, J.-B. Ledeuil, V. Viallet, V. Seznec, and R. Dedryvère, "Interface Stability of Argyrodite Li_6PS_5Cl toward $LiCoO_2$, $LiNi_{1/3}Co_{1/3}Mn_{1/3}O_2$, and $LiMn_2O_4$ in Bulk All-Solid-State Batteries," *Chemistry of Materials* 29 (2017): 3883.

9. B. Pang, Y. Gan, Y. Xia, H. Huang, X. He, and W. Zhang, "Regulation of the Interfaces Between Argyrodite Solid Electrolytes and Lithium Metal Anode," *Frontiers in Chemistry* 10 (2022): 837978.

10. D. Cao, X. Sun, Q. Li, A. Natan, P. Xiang, and H. Zhu, "Lithium Dendrite in All-Solid-State Batteries: Growth Mechanisms, Suppression Strategies, and Characterizations," *Matter* 3 (2020): 57.

11. T. Chen, L. Zhang, Z. Zhang, et al., "Argyrodite Solid Electrolyte with a Stable Interface and Superior Dendrite Suppression Capability Realized by ZnO Co-Doping," *ACS Applied Materials and Interfaces* 11 (2019): 40808.

12. J. Doux, H. Nguyen, D. H. S. Tan, et al., "Stack Pressure Considerations for Room-Temperature All-Solid-State Lithium Metal Batteries," *Advanced Energy Materials* 10 (2020): 1903253.

13. Z. You, C. Zheng, J. Wu, et al., "In Situ Grain Boundary Engineering Enabling Ultralong Stable Cycling Garnet-Based Solid-State Electrolytes," *Nano Letters* 25 (2025): 5110.

14. J. Wu, Z. You, M. Li, et al., "Synergistic Reduction and Oxidation Resistant Interface Modifier for High-Voltage and High-Loading Solid-State Lithium Batteries," *Advanced Energy Materials* 15 (2025): 2403585.

15. Y. Dong, Y. Chen, Q. Zeng, et al., "Challenges and Strategies of Fast-Charging Li-Ion Batteries with a Focus on Li Plating," *Energy Material Advances* 5 (2024): 0113.

16. J. Kasemchainan, S. Zekoll, D. Spencer Jolly, et al., "Critical Stripping Current Leads to Dendrite Formation on Plating in Lithium Anode Solid Electrolyte Cells," *Nature Materials* 18 (2019): 1105.

17. W. Arnold, D. A. Buchberger, Y. Li, M. Sunkara, T. Druffel, and H. Wang, "Halide Doping Effect on Solvent-Synthesized Lithium Argyrodites Li_6PS_5X (X= Cl, Br, I) Superionic Conductors," *Journal of Power Sources* 464 (2020): 228158.

18. W. Arnold, V. Shreyas, Y. Li, et al., "Synthesis of Fluorine-Doped Lithium Argyrodite Solid Electrolytes for Solid-State Lithium Metal Batteries," *ACS Applied Materials and Interfaces* 14 (2022): 11483.

19. C. Wei, R. Wang, Z. Wu, et al., "Dual N-Modification Enables High-Performance Solid-State Li Metal Batteries with $Li_{5.5}PS_{4.5}Cl_{1.5}$," *Chemical Engineering Journal* 476 (2023): 146531.

20. Y. Liu, H. Su, M. Li, et al., "*In Situ* Formation of a Li_3N-Rich Interface between Lithium and Argyrodite Solid Electrolyte Enabled by Nitrogen Doping," *Journal of Materials Chemistry A* 9 (2021): 13531.

21. Y. Huang, S. Chen, Y. Yang, et al., "Unlocking the Potential of Li–Ag Alloys: Phase Selection and Practical Application," *Energy Material Advances* 5 (2024): 0108.

22. X. Ji, S. Hou, P. Wang, et al., "Solid-State Electrolyte Design for Lithium Dendrite Suppression," *Advanced Materials* 32 (2020): 2002741.

23. R. Xu, F. Han, X. Ji, X. Fan, J. Tu, and C. Wang, "Interface Engineering of Sulfide Electrolytes for All-Solid-State Lithium Batteries," *Nano Energy* 53 (2018): 958.

24. W. Tang, N. Shen, X. Xiong, et al., "Competitive Roles of Conductivity and Lithiophility in Composite Lithium Metal Anode," *Energy Material Advances* 5 (2024): 0084.

25. U. Nisar, S. A. J. A. Al-Hail, R. K. Petla, et al., "Understanding the Origin of the Ultrahigh Rate Performance of a SiO_2-Modified $LiNi_{0.5}Mn_{1.5}O_4$ Cathode for Lithium-Ion Batteries," *ACS Applied Energy Materials* 2 (2019): 7263.

26. B. Xu, W. Li, H. Duan, et al., "Li_3PO_4-Added Garnet-Type $Li_{6.5}La_3Zr_{1.5}Ta_{0.5}O_{12}$ for Li-Dendrite Suppression," *Journal of Power Sources* 354 (2017): 68.

27. L. Lin, F. Liang, K. Zhang, H. Mao, J. Yang, and Y. Qian, "Lithium Phosphide/Lithium Chloride Coating on Lithium for Advanced Lithium Metal Anode," *Journal of Materials Chemistry A* 6 (2018): 15859.

28. F. Poulsen, "Ionic Conductivity of Solid Lithium Iodide and Its Monohydrate," *Solid State Ionics* 2 (1981): 53.

29. L. Lin, L. Suo, Y. Hu, H. Li, X. Huang, and L. Chen, "Epitaxial Induced Plating Current-Collector Lasting Lifespan of Anode-Free Lithium Metal Battery," *Advanced Energy Materials* 11 (2021): 2003709.

30. Y. Li, Y. Sun, A. Pei, et al., "Robust Pinhole-Free Li_3N Solid Electrolyte Grown from Molten Lithium," *ACS Central Science* 4 (2018): 97.

31. H. Chen, A. Pei, D. Lin, et al., "Uniform High Ionic Conducting Lithium Sulfide Protection Layer for Stable Lithium Metal Anode," *Advanced Energy Materials* 9 (2019): 1900858.

32. Y. Cui, S. Liu, D. Wang, et al., "A Facile Way to Construct Stable and Ionic Conductive Lithium Sulfide Nanoparticles Composed Solid Electrolyte Interphase on Li Metal Anode," *Advanced Functional Materials* 31 (2021): 2006380.

33. A. P. Maltsev, I. V. Chepkasov, A. G. Kvashnin, and A. R. Oganov, "Ionic Conductivity of Lithium Phosphides," *Crystals* 13 (2023): 756.

34. W. Li, M. Li, S. Wang, et al., "Superionic Conducting Vacancy-Rich β-Li_3N Electrolyte for Stable Cycling of All-Solid-State Lithium Metal Batteries," *Nature Nanotechnology* 20 (2025): 265.

35. L. Hu, T. Yang, X. Yan, et al., "*In Situ* Construction of LiF–Li_3N-Rich Interface Contributed to Fast Ion Diffusion in All-Solid-State Lithium–Sulfur Batteries," *ACS Nano* 18 (2024): 8463.

36. T. Lapp, S. Skaarup, and A. Hooper, "Ionic Conductivity of Pure and Doped Li_3N," *Solid State Ionics* 11 (1983): 97.

37. H. Su, Y. Liu, Y. Zhong, et al., "Stabilizing the Interphase between Li and Argyrodite Electrolyte through Synergistic Phosphating Process for All-Solid-State Lithium Batteries," *Nano Energy* 96 (2022): 107104.

38. R. Pathak, K. Chen, A. Gurung, et al., “Fluorinated Hybrid Solid-Electrolyte-Interphase for Dendrite-Free Lithium Deposition,” *Nature Communications* 11 (2020): 93.

39. K. Chen, R. Pathak, A. Gurung, et al., “Flower-Shaped Lithium Nitride as a Protective Layer via Facile Plasma Activation for Stable Lithium Metal Anodes,” *Energy Storage Materials* 18 (2019): 389.

40. D. K. Singh, A. Henss, B. Mogwitz, et al., “Li_6PS_5Cl Microstructure and Influence on Dendrite Growth in Solid-State Batteries with Lithium Metal Anode,” *Cell Reports Physical Science* 3 (2022): 101043.

41. P. Ren, X. Wang, B. Huang, Z. Liu, and R. Liu, “Li_3N Interlayer Enables Stable Long-Term Cycling for Sulfide-Based All-Solid-State Li Metal Batteries,” *Journal of Energy Storage* 82 (2024): 110200.

42. E. Kazyak, R. Garcia-Mendez, W. S. LePage, et al., “Li Penetration in Ceramic Solid Electrolytes: Operando Microscopy Analysis of Morphology, Propagation, and Reversibility,” *Matter* 2 (2020): 1025.

43. K. Kanamura, H. Tamura, S. Shiraishi, and Z.-I. Takehara, “XPS analysis for the lithium surface immersed in γ-butyrolactone containing various salts,” *Electrochimica Acta* 40 (1995): 913–921.

44. S.-K. Otto, Y. Moryson, T. Krauskopf, et al., “In-Depth Characterization of Lithium-Metal Surfaces with XPS and ToF-SIMS: Toward Better Understanding of the Passivation Layer,” *Chemistry of Materials* 33 (2021): 859.

45. M. Wu, Z. Wen, Y. Liu, X. Wang, and L. Huang, “Electrochemical Behaviors of a Li_3N Modified Li Metal Electrode in Secondary Lithium Batteries,” *Journal of Power Sources* 196 (2011): 8091.

46. W. Li, G. Wu, C. M. Araújo, et al., “Li+ Ion Conductivity and Diffusion Mechanism in α-Li_3N and β-Li_3N,” *Energy and Environmental Science* 3 (2010): 1524.

47. K. P. C. Yao, D. G. Kwabi, R. A. Quinlan, et al., “Thermal Stability of Li_2O_2 and Li_2O for Li-Air Batteries: In Situ XRD and XPS Studies,” *Journal of the Electrochemical Society* 160 (2013): A824.

48. J. Sharma, T. Gora, J. D. Rimstidt, and R. Staley, “X-Ray Photoelectron Spectra of the Alkali Azides,” *Chemical Physics Letters* 15 (1972): 232.

49. D. Cheng, T. A. Wynn, X. Wang, et al., “Unveiling the Stable Nature of the Solid Electrolyte Interphase between Lithium Metal and LiPON via Cryogenic Electron Microscopy,” *Joule* 4 (2020): 2484.

50. K. N. Wood, and G. Teeter, “XPS on Li Battery Related Compounds: Analysis of Inorganic SEI Phases and a Methodology for Charge Correction,” *ACS Applied Energy Materials* 1 (2018): 4493–4504.

51. J. Auvergniot, A. Cassel, D. Foix, V. Viallet, V. Seznec, and R. Dedryvère, “Redox Activity of Argyrodite Li_6PS_5Cl Electrolyte in All-Solid-State Li-Ion Battery: An XPS Study,” *Solid State Ionics* 300 (2017): 78.

52. C. Liu, T. Li, H. Zhang, et al., “DMF Stabilized Li_3N Slurry for Manufacturing Self-Prelithiatable Lithium-Ion Capacitors,” *Science Bulletin* 65 (2020): 434.

53. G. Jiang, J. Liu, J. He, et al., “Hydrofluoric Acid-Removable Additive Optimizing Electrode Electrolyte Interphases with Li^+ Conductive Moieties for 4.5 V Lithium Metal Batteries,” *Advanced Functional Materials* 33 (2023): 2214422.

54. K. Kanamura, H. Tamura, and Z. Takehara, “XPS Analysis of a Lithium Surface Immersed in Propylene Carbonate Solution Containing Various Salts,” *Journal of Electroanalytical Chemistry* 333 (1992): 127.

55. H. Hosokawa, “ Tolerance for Li Dendrite Penetration in Ta-doped $Li_7La_3Zr_2O_{12}$Solid Electrolytes Sintered with $Li_{2.3}C_{0.7}B_{0.3}O_3$ Additive,“ *Materials Letters* 4 (2020).

56. A. Morchhale, Z. Tang, R. Ghahremani, R. Farahati, and J.-H. Kim, “Re-Evaluating Critical Current Density in Solid-State Batteries: Challenges and Proposing an Alternative,” *Journal of Power Sources* 624 (2024): 235605.

57. S. Yubuchi, S. Teragawa, K. Aso, K. Tadanaga, A. Hayashi, and M. Tatsumisago, “Preparation of High Lithium-Ion Conducting Li_6PS_5Cl Solid Electrolyte from Ethanol Solution for All-Solid-State Lithium Batteries,” *Journal of Power Sources* 293 (2015): 941.

58. Z. Tang, A. Morchhale, J. R. Sayre, and J.-H. Kim, “In-Situ Electrochemical Characterization of Dynamic Void Formation and Lithium Dendrite in All-Solid-State Batteries,” *Journal of Energy Storage* 107 (2025): 114966.

59. K. Pan, F. Zou, M. Canova, Y. Zhu, and J.-H. Kim, “Comprehensive Electrochemical Impedance Spectroscopy Study of Si-Based Anodes Using Distribution of Relaxation Times Analysis,” *Journal of Power Sources* 479 (2020): 229083.

60. J. Pan, Q. Zhang, X. Xiao, Y.-T. Cheng, and Y. Qi, “Design of Nanostructured Heterogeneous Solid Ionic Coatings through a Multiscale Defect Model,” *ACS Applied Materials and Interfaces* 8 (2016): 5687.

61. A. L. Davis, E. Kazyak, D. W. Liao, K. N. Wood, and N. P. Dasgupta, “Operando Analysis of Interphase Dynamics in Anode-Free Solid-State Batteries with Sulfide Electrolytes,” *Journal of the Electrochemical Society* 168 (2021): 070557.

62. A. Orue Mendizabal, M. Cheddadi, A. Tron, A. Beutl, and P. López-Aranguren, “Understanding Interfaces at the Positive and Negative Electrodes on Sulfide-Based Solid-State Batteries,” *ACS Applied Energy Materials* 6 (2023): 11030.

63. B. D. Dandena, W.-N. Su, D.-S. Tsai, et al., “Li–Sb Alloy Formation Strategy to Improve Interfacial Stability of All-Solid-State Lithium Batteries,” *Small Methods.* (2025): 2400571.

64. Y.-H. Wang, J. Yue, W.-P. Wang, et al., “Constructing a Stable Interface between the Sulfide Electrolyte and the Li Metal Anode via a Li+-Conductive gel Polymer Interlayer,” *Materials Chemistry Frontiers.* (2021): 10.1039.D1QM00395J.

65. H. Erabhoina and M. Thelakkat, “Tuning of Composition and Morphology of $LiFePO_4$ Cathode for Applications in All Solid-State Lithium Metal Batteries,” *Scientific Reports* 12 (2022): 5454.

66. B. W. Taklu, W.-N. Su, Y. Nikodimos, et al., “Dual CuCl Doped Argyrodite Superconductor to Boost the Interfacial Compatibility and Air Stability for All Solid-State Lithium Metal Batteries,” *Nano Energy* 90 (2021): 106542.

67. Y. Zhou, C. Doerrer, J. Kasemchainan, P. G. Bruce, M. Pasta, and L. J. Hardwick, “Observation of Interfacial Degradation of Li_6PS_5Cl against Lithium Metal and $LiCoO_2$ via *In Situ* Electrochemical Raman Microscopy,” *Batteries and Supercaps* 3 (2020): 647.

68. K. Ohara, A. Mitsui, M. Mori, et al., “Structural and Electronic Features of Binary Li_2S-P_2S_5 Glasses,” *Scientific Reports* 6 (2016): 21302.

69. H. B. Ribeiro, M. A. Pimenta, and C. J. S. de Matos, “Raman Spectroscopy in Black Phosphorus,” *Journal of Raman Spectroscopy : Jrs* 49 (2018): 76.

70. D. Yuan, J. Cheng, G. Qu, et al., “Amorphous Red Phosphorous Embedded in Carbon Nanotubes Scaffold as Promising Anode Materials for Lithium-Ion Batteries,” *Journal of Power Sources* 301 (2016): 131.

71. C.-Y. Yu, J. Choi, J. Dunham, et al., “Time-Resolved Impedance Spectroscopy Analysis of Aging in Sulfide-Based All-Solid-State Battery Full-Cells Using Distribution of Relaxation Times Technique,” *Journal of Power Sources* 597 (2024): 234116.

72. C. Lee, J. Y. Kim, K. Y. Bae, et al., “Enhancing Electrochemomechanics: How Stack Pressure Regulation Affects All-Solid-State Batteries,” *Energy Storage Materials* 66 (2024): 103196.

73. Y.-J. Kim, R. Rajagopal, S. Kang, and K.-S. Ryu, “Novel Dry Deposition of $LiNbO_3$ or Li_2ZrO_3 on $LiNi_{0.6}Co_{0.2}Mn_{0.2}O_2$ for High Performance All-Solid-State Lithium Batteries,” *Chemical Engineering Journal* 386 (2020): 123975.

74. X. Li, L. Jin, D. Song, et al., “$LiNbO_3$-Coated $LiNi_{0.8}Co_{0.1}Mn_{0.1}O_2$ Cathode with High Discharge Capacity and Rate Performance for All-Solid-State Lithium Battery,” *Journal of Energy Chemistry* 40 (2020): 39.

75. P. Vadhva, J. Hu, M. J. Johnson, et al., “Electrochemical Impedance Spectroscopy for All-Solid-State Batteries: Theory, Methods and Future Outlook,” *ChemElectroChem* 8 (2021): 1930.

76. T. Krauskopf, H. Hartmann, W. G. Zeier, and J. Janek, “Toward a Fundamental Understanding of the Lithium Metal Anode in Solid-State Batteries—An Electrochemo-Mechanical Study on the Garnet-Type Solid Electrolyte $Li_{6.25}Al_{0.25}La_3Zr_2O_{12}$,” *ACS Applied Materials and Interfaces* 11 (2019): 14463.

77. S. Choi, M. Jeon, B.-K. Kim, B.-I. Sang, and H. Kim, “Electrochemical Behaviors of Li-Argyrodite-Based All-Solid-State Batteries under Deep-Freezing Conditions,” *Chemical Communications* 54 (2018): 14116.

78. L. Peng, H. Ren, J. Zhang, et al., “$LiNbO_3$-Coated $LiNi_{0.7}Co_{0.1}Mn_{0.2}O_2$ and Chlorine-Rich Argyrodite Enabling High-Performance Solid-State Batteries under Different Temperatures,” *Energy Storage Materials* 43 (2021): 53.

79. T. H. Wan, M. Saccoccio, C. Chen, and F. Ciucci, “Influence of the Discretization Methods on the Distribution of Relaxation Times Deconvolution: Implementing Radial Basis Functions with DRTtools,” *Electrochimica Acta* 184 (2015): 483.

Supporting Information

Additional supporting information can be found online in the Supporting Information section.